Clays and Clay Minerals, Vol. 60, No. 6, 616–632, 2012.

LABORATORY-SIMULATED DIAGENESIS OF NONTRONITE

MATTHEW A. MILLER, ANDREW S. MADDEN*, MEGAN ELWOOD MADDEN, AND R. DOUGLAS ELMORE
School of Geology and Geophysics, University of Oklahoma, 100 East Boyd Street, Suite 710, Norman, OK 73019, USA

Abstract—Nontronite NAu-1 was exposed to moderate temperature and pressure conditions (250 and 300ºC at 100 MPa pressure) in KCl brine to simulate burial diagenetic systems over accelerated time periods appropriate for laboratory experiments. Powder X-ray diffraction and transmission electron microscopy analysis of the coexisting mixed-layer and discrete 10 Å clay reaction products, and inductively coupled plasma-mass spectrometry analysis of the remaining fluids, indicated that the clay retained octahedral Fe and was identified as Fe-celadonite. The release of Fe from smectite during burial diagenesis has been hypothesized as a mechanism for magnetite authigenesis. High Al activity relative to Fe may be critical to the formation of an aluminous illite and any associated authigenic magnetite.

Key Words—Diagenesis, Ferroceladonite, Illite-Smectite, Iron, Nontronite, TEM, XRD.

INTRODUCTION

Illitization during burial diagenesis is pervasive throughout the rock record in basins of different genetic origins (Hower *et al.*, 1976). In the smectite-to-illite transition, crystals of the smectite group (hydrated, expandable, low-layer charge phyllosilicates) convert to illite, a higher-charge K-saturated phyllosilicate mineral with a collapsed interlayer (Moore and Reynolds, 1997). The greater negative charge in the illite tetrahedral sheet is due to Al substitution for Si. In addition, illite has a more limited range of ions that are allowed in the crystal structure. The dioctahedral sheet consists predominantly of Al-O(H) octahedra, such that Mg^{2+}, Fe^{2+}, and Fe^{3+}, *etc*. from smectites are not incorporated into illite in appreciable quantities. As a result, chlorites and Mg-Fe carbonates are commonly observed coincident with illitization (*e.g.* Elsinger and Pevear, 1988; Rask *et al.*, 1997). Illitization is also a useful indicator of basin history, providing insight into the timing of hydrocarbon maturation and migration (Pevear, 1999).

Aluminum-rich rocks dominate continental clay-forming environments on Earth. Relatively little experimental attention has been given to understanding analogous 'illitization' processes, *i.e*. the formation of ~10 Å clays, by alteration of Fe-rich smectite. Fe-rich smectites such as nontronite and ferrous saponites have been studied in the context of reactivity with contaminants (*e.g.* Jaisi *et al.*, 2008), serving as a terminal electron acceptor for biological processes (*e.g.* Kim *et al.*, 2003; Li *et al.*, 2004; O'Reilly *et al.*, 2005; Ribeiro *et al.*, 2009), and alteration of basalts in oceanic crust (*e.g.* Seyfried and Bischoff, 1979; Andrews, 1980; Köhler *et al.*, 1994; D'Antonio and Kristensen, 2005; Paul *et al.*, 2006), ocean island settings (*e.g.* Dekov *et al.*, 2007; Mas *et al.*, 2008), continental flood basalts (*e.g.* Allen and Scheid, 1946; Keeling *et al*., 2000), and on Mars (*e.g.* Chevrier *et al.*, 2007; Mustard *et al.*, 2008; Ehlmann *et al.*, 2011). Nontronites are also associated with oxidative weathering of sulfides (*e.g.* Fernández-Caliani *et al.*, 2004). Despite the presence of nontronites in diverse environments susceptible to hydrothermal alteration and/or diagenesis, experimental studies of nontronite alteration are lacking. In the summary of experimental illitization studies by Ferrage *et al.* (2011), the starting materials included aluminous bentonites or glasses, montmorillonites, beidellites, or feldspar. Exceptions include Mg-saponite converted to mixed-layer talc/saponite by Eberl *et al.* (1978) and "tri-octahedral vermiculite" converted to "vermiculite and an interstratified phase" by Inoue (1983).

Studies of nontronite 'illitization' to date have focused on the influence of microbes at low temperatures. Biotically induced illitization during early diagenesis may be an important geochemical phenomenon, and has been demonstrated in laboratory experiments simulating shallow burial (*e.g.* Kim *et al.*, 2004), including with nontronite NAu-2 (Zhang *et al.*, 2007; Jaisi *et al.*, 2011). Various bacteria are capable of using Fe either in phyllosilicates or present in other phases as a terminal electron acceptor for anaerobic respiration (Kostka *et al.*, 1999; Stucki and Kostka, 2006), while in other cases Fe^{3+}-bearing smectites may be reduced chemically by metabolic by-products. Certainly, biological dissolution of clays contributes to Fe and silica cycling (*e.g.* Vorhies and Gaines, 2009).

However, abiotic processes are likely to be dominant at depth due to low nutrient circulation, a function of compaction (Lovley and Chapelle, 1995). Ultimately, continued burial reduces fluid and volume reduction and produces mineral-structure reorganization by 2–3 km depth, the observed zone of near universal illitization (Potter *et al*., 2005). Correlation of illitization with increasing depth is commonly observed in powder X-ray

* E-mail address of corresponding author:
amadden@ou.edu
DOI: 10.1346/CCMN.2012.0600607

diffraction (XRD) patterns of sediment cores (*e.g.* Weaver, 1960). In natural systems, illitization usually occurs before temperatures of buried sediments exceed 200ºC, but over periods of up to thousands of years. Illitization proceeds as a function of both temperature and time; as a practical consequence, experiments simulating burial diagenesis at higher temperatures can accomplish illitization in timescales accessible for laboratory studies, as demonstrated in the present study.

Historically, mechanisms proposed for burial illitization have been divided into two groups (*e.g.* Altaner and Ylagan, 1997): solid state transformation continuum from smectite to illite through gradually increasing illite-smectite layer ordering (Hower *et al*., 1976; Eslinger and Pevear, 1988), or smectite dissolution providing source material for illite precipitation (Ahn and Peacor, 1986). Abercrombie *et al.* (1994) offered a variation on the dissolution-precipitation mechanism, suggesting aluminum mobilized by the dissolution of kaolinite in conjunction with K-saturated smectites results in illite precipitation. More recently, McCarty *et al.* (2008, 2009) and Lanson *et al.* (2009) argued that multiple illite-smectite mixed-layer phases coexist simultaneously in close proximity, depending on local chemical gradients that prompt layer collapse and illitization. Thus, the Fe distribution between mineral and solution phases is linked to the fate of all the other chemical components of the system. Experimental diagenesis of nontronite might, therefore, lead to mixed-layer nontronite-illite-like phases, followed by illite + Fe oxides, if enough Al is incorporated following release from decomposed kaolinite. On the other hand, if limited Al is incorporated, mixed-layer nontronite-celadonite-like phases followed by celadonite would be expected. Celadonites are a common 10 Å phase found in veins and vugs associated with hydrothermal alteration of basaltic or andesitic rock (Odom, 1984).

The potential release of Fe from smectite during diagenesis would have wide consequences for interpretation of rock magnetic signatures that can be used to infer time and temperature paths for fluid alteration. When a diagenetic process results in the retention of a magnetic field, the resultant magnetic memory-chemical remanent magnetization (CRM) is the fundamental rock magnetic property used to investigate timing of depositional and diagenetic events. The CRM associated with authigenic magnetite occurs in units of varied lithologies such as sandstones (*e.g.* Elmore and Leach, 1990), limestones (*e.g.* McCabe *et al.*, 1983), and shales (*e.g.* Dennie *et al.*, 2012). Even trace concentrations of magnetite can host a magnetic remanence, or the retention of a relict magnetic field's magnitude and orientation. Paleomagnetic studies have helped derive chronostatic continental positions and determine timing of geochemical events throughout the geologic record.

If a CRM is housed in magnetite, and if the magnetite is derived from chemical processes during diagenesis, then a source of Fe must either be mobilized from existing mineralogy or transported to the host rock following deposition. Because the CRM recorded in magnetite often appears coincident with transformation of expandable smectite clays to non-expandable illite, the precipitation of magnetite or other Fe-containing phases could be the result of clay alteration.

Most previous studies have assumed the development of CRM through magnetite authigenesis is linked to pyrite oxidation (Banerjee *et al.*, 1997) resulting from complexation with organics (Brothers *et al.*, 1996; Blumstein *et al.*, 2004), hematite/Fe oxide reduction *via* hydrocarbon migration (Elmore *et al.*, 1987; McCabe *et al.*, 1987), or the input of orogenic fluids (*e.g.* Elmore *et al.*, 2001). Field and laboratory studies have verified that pyrite can be converted to magnetite when exposed to clay diagenetic temperatures (Brothers *et al.*, 1996; Suk *et al.*, 1990a, 1990b; Jackson *et al.*, 1988; Blumstein *et al.*, 2004; Moreau *et al.*, 2005). Preservation of organic matter that could mediate pyrite oxidation during diagenesis is probably dictated by organic sorption onto clay-mineral surfaces (Kennedy *et al.*, 2002).

Rock magnetic, paleomagnetic, and clay mineralogy studies support the coincidence of magnetite authigenesis and the transformation of smectite to illite even without the input of external fluids or pyrite oxidation (Katz *et al.*, 1998, 2000; Cogoini, 2001; Gill *et al.*, 2002; Zegers *et al.*, 2003). Several studies have reported an agreement between the paleomagnetic date for magnetite authigenesis and K-Ar dating of illite (*e.g.* Elliot *et al.*, 2006; Tohver *et al.*, 2008; Zwing *et al.*, 2009). Direct observations of magnetite in association with clay minerals by electron microscopy have been limited, partly due to the difficulty of imaging nanoscale grains by scanning electron microscopy (SEM) and microprobe methods. Microscope studies have mainly implicated sulfide oxidation to magnetite. Weil and Van der Voo (2002) noted the presence of microscale Fe oxides in a matrix of Fe-rich smectite and aluminous illite; however, most of the CRM signal clearly resulted from oxidized pyrite. Following experimental heating of clay-rich rocks, Moreau *et al.* (2005) found that magnetite identified by rock magnetism could not be identified by SEM, but its abundance correlated with pyrite in the groundmass. Woods *et al.* (2002) noted a spatial correlation between the distribution of magnetite-hosted CRM and illitization in Jurassic sediments impacted by nearby igneous activity, but also documented SEM evidence that Fe sulfide converted to magnetite. Relatively little experimental evidence supports phyllosilicate transformations leading to magnetite authigenesis, without pyrite. Hirt *et al.* (1993) synthesized magnetite experimentally from Fe oxides sorbed to clay mineral surfaces at temperatures above 250ºC and atmospheric pressure. However, investigations of Fe-rich smectites that contribute to an understanding of

https://doi.org/10.1346/CCMN.2012.0600607 Published online by Cambridge University Press

whether or not 'structural' Fe in smectite can be released from smectite during illitization and precipitate as magnetite are lacking.

In the present study, hydrothermal experiments were conducted on the Fe-rich smectite, nontronite NAu-1, with KCl brines in cold-seal gold capsules at 100 MPa and 250–300ºC to test these models of illitization using smectites with structurally bound Fe. Elevated temperatures were used as a proxy for lower-temperature systems over longer timescales, such as was shown for Al-rich clays by Ferrage *et al.* (2011). NAu-1 was size-fractionated and treated with citrate-bicarbonate-dithionite (CBD) to remove all initial surface-loaded Fe. Unreacted NAu-1 and the experimental products were examined for evidence of illitization and Fe mobilization *via* powder XRD, transmission electron microscopy (TEM), and the residual aqueous fluid analyzed by inductively coupled plasma mass spectrometry (ICP-MS).

MATERIALS AND METHODS

Special Clay NAu-1

The Clay Minerals Society (CMS) Special Clay, Nontronite NAu-1, was obtained from the CMS Source Clays Repository. The full-cell structural formula of NAu-1 is $M^{+}_{1.05}[Al_{.29}Fe_{3.68}Mg_{.04}][Si_{6.98}Al_{1.02}]O_{20}(OH)_4$, where M^{+} is the exchangeable interlayer cation (divalent cation occupancy is reduced to 0.55 formula units) (Keeling *et al*., 2000). NAu-1 was chosen because it has been well characterized, facilitating direct comparison of results with other studies. However, well characterized, source and special clays are natural materials and are composed of mixtures of heterogeneous phases (Chipera and Bish, 2001). Therefore, physical and chemical treatment of NAu-1 to remove comingled contaminants such as quartz, kaolinite, biotite, and Fe-oxide phases preceded use in illitization experiments.

Physical removal of the gross non-clay phase contamination from NAu-1 began by gently disaggregating clumps of the untreated clay *via* mortar and pestle. Manual removal of large particulate non-clay minerals was accomplished with tweezers and sifting on filter paper. The relatively large, platy biotite stuck to the paper, while the fine-grained fraction, including the clay, quartz, and Fe oxides, did not. Following these treatments, the remaining material was water saturated for 24 h, and then dispersed *via* an ultrasonic bath for 1 h, breaking up agglomerations of mineral grains, and suspending the fine grains within the water column. After settling for 16 h only fine-grained material remained suspended in the supernatant, which was decanted and centrifuged. Multiple sonication-centrifugation sequences were combined into a single clay aliquot prior to further treatment. X-ray diffraction of the clay separates from this stage indicated effective removal of residual quartz and calcite, and almost complete removal of biotite, but not goethite.

Chemical removal of the goethite (and other trace Fe-oxide phases) was accomplished *via* the CBD methods of Bartels (1996) and Ulrey and Drees (2008), except that phosphate dispersants were avoided to limit contamination of the system with potentially interfering species. Special care was taken not to exceed 80ºC during the digestion process, thereby avoiding the formation of sulfide precipitates. The clay color indicated that Fe within the clay-mineral structure was also reduced, but retained octahedral occupancy and slowly re-oxidized upon exposure to air. Following reduction, the reduced clay was separated *via* centrifugation, dispersed with ultrapure water in an ultrasonic bath, centrifuged three times to remove residual digestion chemicals, and dried at 50ºC. The resulting material was bright yellow-green, indicative of relatively complete re-oxidation (Stucki, 2011).

No effort was made to remove the kaolinite. The similarity to nontronite in terms of crystal size, chemistry, and morphology would probably have made separation difficult. More importantly, the kaolinite provided an aluminum and silica source for illitization experiments.

Size separation to extract the $\leqslant 0.2$ μm size fraction was performed *via* centrifugation. In practice, centrifugation was capable of separating only the $\leqslant 2$ μm size fractionation (not the initially desired $\leqslant 0.2$ μm fraction) as verified by TEM investigation, probably a result of omitting the Na-hexametaphosphate dispersant from the centrifugation step described by Ulrey and Drees (2008). Following centrifugation, clay separates were dried at 60ºC and disaggregated gently with an agate mortar and pestle.

Powder XRD

X-ray diffraction was used as the primary screening characterization tool to determine success of the clay purification process and assess the degree of illitization in experimental samples. Diffraction patterns were collected using a Rigaku Ultima IV X-ray diffractometer with Bragg Brentano beam geometry, goniometer radius of 285 mm, CuKα radiation (λ = 1.5418 Å), and either a Ni filter with a silicon strip detector or a fixed graphite monochromator with a scintillation counter.

Powder mounts were analyzed using the scintillation counter or silicon strip detector depending on the needs of the analysis. Oriented aggregate clay specimens were analyzed using a scintillation counter and variable slits. Counting was performed for 2 s at 0.02º/step through a 2θ range of 2–70º. Random powder analyses were performed using a silicon strip detector and fixed slits. Counting was performed at 10º/min in 0.02º scan widths through a 2θ range of 3–65º. Tube settings for both setups were 40 kV accelerating voltage, 44 mA heating amperage, and 1.76 kW load. The XRD data analysis and simulation were performed using *PDXL* version 1.6.0.1, and *MDI Jade* version 9.1 software and associated powder diffraction databases.

https://doi.org/10.1346/CCMN.2012.0600607 Published online by Cambridge University Press

The clay-mineral crystal size was estimated by both the Scherrer method from XRD patterns and through examination of TEM images. The Scherrer crystallite size from basal peaks in air-dried oriented aggregate mounts was divided by the appropriate crystal-domain thickness: 15.2 Å assuming two waters of hydration for nontronite, and 7.2 Å for poorly crystalline kaolinite.

The TEM provides a different perspective on crystallite size. The undulatory habit of smectite at the nanoscale (*i.e.* Figure 1) presents only a fraction of the actual crystallite in the Bragg condition necessary for XRD. Only a 100 Å section of a curviplanar 200 Å nontronite crystal may be probed by the X-ray beam, while the same crystal may be observed in its entirety *via* the TEM. In addition, XRD peak breadth is a function of all crystallite sizes in the Bragg condition, and any size estimate made from FWHM values will reflect an average size. In comparison, TEM imaging is very much a point-measurement technique.

TEM

The TEM analysis of NAu-1 separates was used to gauge the success of purification before experimentation, assess the degree of illitization after reaction, and identify potential Fe-oxide phases. In addition, crystal morphology was examined *via* bright-field imaging at relatively low magnification (20–100 kX) to identify mineralogy and textural features in each sample.

Bright-field images, electron diffraction, and energy-dispersive spectra (EDS) were collected for NAu-1 mounted on 400 mesh/in lacey carbon-coated copper TEM grids. Clay suspensions were applied to the surface of the TEM grid *via* pipette, and the clay particulates deposited by drawing the suspension through the grid with a piece of dry filter paper or laboratory tissue.

Lattice-fringe observations were made on NAu-1 embedded in LR White acrylic resin to limit interlayer collapse induced by electron microscope column heating and vacuum. Intercalation was performed in uncured resin *via* ultrasonication for 1 h followed by rotational mixing for an additional 48 h in a 1 mL sealed microcentrifugation vial. Following intercalation, samples were polymerized in a 60ºC oven for 24 h. Cured clay containing resin was rough blocked with a knife, mounted on a resin stub with cyanoacrylate glue, faced with a razor blade, and thin sectioned with a glass knife on an AO Reichart Ultracut Ultramicrotome. Sections were mounted on 200 mesh/in copper TEM grids.

Imaging was conducted at the Sam Noble Roberts Electron Microscopy lab at the University of Oklahoma. Bright field and electron diffraction imaging was performed using a JEOL 2000FX TEM with a LaB_6 source at 200 kV accelerating voltage utilizing a 120 µm condensing lens aperture and 50 µm objective aperture, and various selected area electron diffraction (projector) apertures. A tungsten field emission-sourced JEOL 2010 F HRTEM at 200 kV accelerating voltage was used for bright-field imaging and EDS.

Cold-seal experiments

Dried NAu-1 and 2 M potassium chloride or 2 M potassium and Fe chloride solutions were loaded into gold tubing for cold-seal experiments at either 250 or 300ºC and 100 MPa after Ferrage *et al.* (2011) (Table 1). Sample names indicate heating temperature and the addition of graphite and or $FeCl_2$ brine *via* the identifiers (C) and (F), respectively. Preliminary experiments at 150ºC showed no illitization after 2 weeks, and thus only higher temperatures were considered further. Also, the results of Ferrage *et al.* (2011) demonstrated higher temperatures could reasonably reproduce trends from rocks experiencing progressive burial diagenesis. Half the experiments contained graphite as a reductant, which is oxidized to form CO_2-rich fluids in the presence of water at these experimental temperature, pressure, and duration conditions (Holloway, 1984), analogous to the likely environment at burial depth (Lovely and Chapelle, 1995). The clay solid:solution mass ratio was kept at

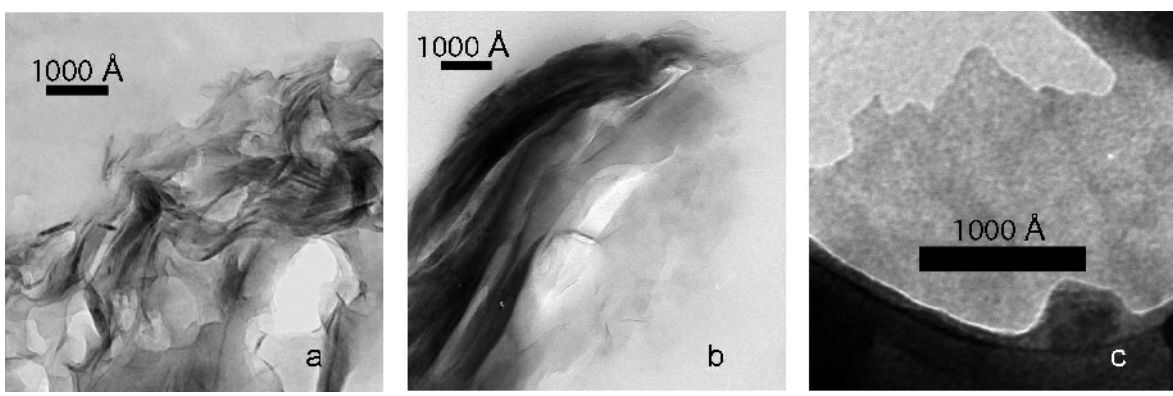

Figure 1. TEM images of NAu-1 following physical and chemical treatment. Nontronite particles consisted of laminated curviplanar crystal aggregates approaching 1 µm in size. Characteristic nontronite textures included (a) crumpled habit, (b) locally curved sheets, and (c) irregular sheet borders.

https://doi.org/10.1346/CCMN.2012.0600607 Published online by Cambridge University Press

Table 1. Cold-seal experimental conditions. Post-experiment fluid extraction and digestion completed *via* pipette immediately upon opening sample capsule.

Sample	Mass (mg)	Solution type	Solution mass (mg)	Graphite mass (mg)	Extraction volume (μL)
250	5.64	KCl	53.69		20
300	8.27	KCl	55.82		15
250 C	2.93	KCl	28.90	0.34	15
300 C	4.53	KCl	19.10	0.75	
250 F	8.16	KCl + $FeCl_2$	62.59		
300 F	6.05	KCl + $FeCl_2$	68.31		
250 FC	3.06	KCl + $FeCl_2$	44.86	0.18	
300 FC	6.06	KCl + $FeCl_2$	38.56	0.05	
NAu-1					15

~1:10 to promote hydrothermal illitization (Huang *et al.*, 1993). Individual capsules were crimped at one end and sealed with an argon plasma arc weld. Prior to loading reagents, a plastic loading sleeve was inserted into the gold tube, covering the open end of the tube to prevent clay or salt solution from clinging to the metal surface and contaminating the weld. Granulated clay and graphite powder were added with a small aluminum scoop through the plastic sleeve, then the sleeve was withdrawn and the solid masses were verified *via* an electronic balance. After massing, the sleeve was re-inserted to cover the mouth of the gold tube, KCl and $FeCl_2$ brines added *via* a gas-tight chromatography syringe, and the added mass verified *via* electronic balance. After loading, the plastic sleeve was withdrawn, the open capsule end crimped, the tube frozen *via* aerosol jet to prevent volatilization of the solutions, and the capsule welded shut. Capsules were then placed in an oven at ~120ºC for 15 min, and re-weighed as a leak test. Experiments were conducted in subhorizontal NIMONIC 105® cold-seal pressure vessels at 100 MPa. Temperature was monitored with an internal Chromel-Alumel thermocouple, and pressure was monitored with a factory-calibrated bourdon tube gauge; the uncertainties in temperature and pressure were <10ºC and <10 MPa, respectively. After 2 weeks, samples were air quenched at ~75ºC/min, and massed immediately as a leak test. No leaking capsules were identified before or after the experimental run.

Once fluid extraction was complete, the gold capsules were opened with shears, and the clays extracted *via* spatula and $CaCl_2$ irrigation. The illitization products were caked together, requiring ultrasonic disaggregation for ~15 min to disperse the clay and encourage intercalation of the Ca^{2+} ions in solution. Intercalation was conducted for 3 days, following which time the suspensions were centrifuged, decanted, and rinsed with ultrapure water *via* centrifugation twice to remove excess salts. Ca^{2+} exchange was preferred to K^+ to encourage glycol uptake, thereby avoiding misidentification of dehydrated smectite structures as illite (Ferrage *et al.*, 2011).

Aqueous chemical analysis

Following quenching, 15–20 μL of the fluid was extracted from samples for Al, Si, and Fe analysis using ICP-MS at the University of Texas at Arlington. Samples that included $FeCl_2$ were not analyzed *via* ICP, as the added Fe would overwhelm the signal of that released from the clay mineral. The results from these extracts were intended to detect aqueous Al, Si, and Fe released from NAu-1, but not precipitated in a solid phase, during illitization. The fluid volume extracted was based on the maximum that could be removed without entraining experimental solids with an adjustable pipettor. Each gold tube was cleaned, and then dented with a plastic implement to create a trough into which the liquid aliquot could flow when the tube was punctured with a needle. Upon puncturing, the fluids flowed under pressure into the trough. Each sample was collected and immediately digested in 1% nitric acid (Table 1), in addition to an ultrapure water blank. Unreacted NAu-1 saturated in KCl brine for the duration of the pressure and temperature experiments at ambient conditions served as a control sample.

RESULTS

NAu-1 characterization

Clay crystallite sizes of 100–180 Å for nontronite and 115–315 Å for kaolinite are based on examination of the (*hk*0) peaks from XRD patterns of randomly oriented clay powder after purification and disaggregation in a mortar and pestle. The average crystal-domain thickness (N) of purified NAu-1 was 10 and 46 domains for nontronite and kaolinite, respectively. The TEM-based crystallite size estimates for NAu-1 ranged from 100 to 5000 Å for nontronite, and no kaolinite was identified. The general agreement of crystallite sizes from powder XRD and TEM images indicated that the visually measured fraction was representative of the bulk properties of NAu-1, despite the statistically much smaller number of observations. Somewhat larger estimates from TEM image analyses compared to those based on XRD patterns were probably due to clay morphology and the nature of XRD analysis (Figure 1).

https://doi.org/10.1346/CCMN.2012.0600607 Published online by Cambridge University Press

Reaction products

The solids from experiments with added Fe (samples 250 F, 300 F, 250 FC, and 300 FC) turned red upon opening. The redox reaction observed indicates that a reducing environment existed in the tubes during the experiment, with or without added graphite. Reducing conditions improve the likelihood that if Fe were released from the phyllosilicate structure, it would probably remain in aqueous solution rather than precipitate. The formation of magnetite requires a sufficient supply of ferric and ferrous Fe. The XRD patterns of these samples contained low-intensity peaks appropriate for hematite, the presence of which was considered an experimental artifact and was disregarded during examination of these samples *via* TEM.

Powder XRD

When viewed in increasing temperature sequence, all oriented mounts displayed increasing illitization from parent nontronite to 250ºC and then to 300ºC, irrespective of the addition of graphite or $FeCl_2$ solution. Conversion of nontronite to an R3 ordered mixed-layer phase was indicated by the collapse of low-order d_{001} and d_{002} basal nontronite peaks towards 10 Å, and the progressive shift of the d_{003} nontronite peak to 5.09 Å as the mixed-layer $d_{002/003}$ composite peak. The d_{001} and d_{002} peaks of glycolated NAu-1, 16.9 Å and 8.66 Å, respectively, shifted toward 10 Å, indicating increasing I-S content (Figures 2–5). The I-S $d_{002/003}$ peak was of low intensity, a result of destructive interference caused by the X-ray scattering effect of the dense electron clouds surrounding octahedral Fe; however, the $d_{002/003}$ peaks shifted toward 5.0 Å (17.7º2θ) through the heating sequences, indicative of an illite content in mixed-layer I-S of ~75% at 250ºC and ~90% at 300ºC, using Wantanabe's method (mentioned by Moore and Reynolds, 1997). Środoń's (1980) Δ2θ method, measuring the angle between the $d_{001/002}$ and $d_{002/003}$ peaks, yielded similar results (Table 2). A discrete illite-like phase was also probably present in experimental samples, given either a distinct hump or shoulder at 10 Å within the I-S $d_{001/002}$ peak. Coexisting mixed-layer and discrete 10 Å clay phases within the experimental system are consistent with the chemical gradient illitization model (*e.g.* McCarty *et al.*, 2009).

The kaolinite peaks at 7.17 and 3.57 Å (12.32 and 24.92º2θ) and the broad intensity plateau between 4.55 and 3.57 Å present in NAu-1 disappeared upon heating to 250ºC in all samples except 250 F. Kaolinite decomposition was complete in all samples by 300ºC. Diffraction peaks corresponding to halite and sylvite were found to some degree in all the heated experimental samples. Halite contamination was probably due to incomplete K^+ for Na^+ interlayer exchange prior to cold-seal experimentation, the original source of Na being CBD reactants. A beneficial side effect of these non-expandable crystalline contaminants was the ability to accurately fix the XRD patterns in 2θ space and correct sample displacement. Investigation of the XRD mounts *via* optical microscopy showed nearly cubic crystal forms within the clay, indicating crystallization of the salts after the clay was deposited on the glass slides. Halide crystal growth 'upended' the clay crystallites, decreasing their preferred orientation and allowing identification of clay mineral (*hk*0) peaks and the ability to make a more detailed mineralogical assignment. The XRD patterns of air-dried samples showed that the 10 Å

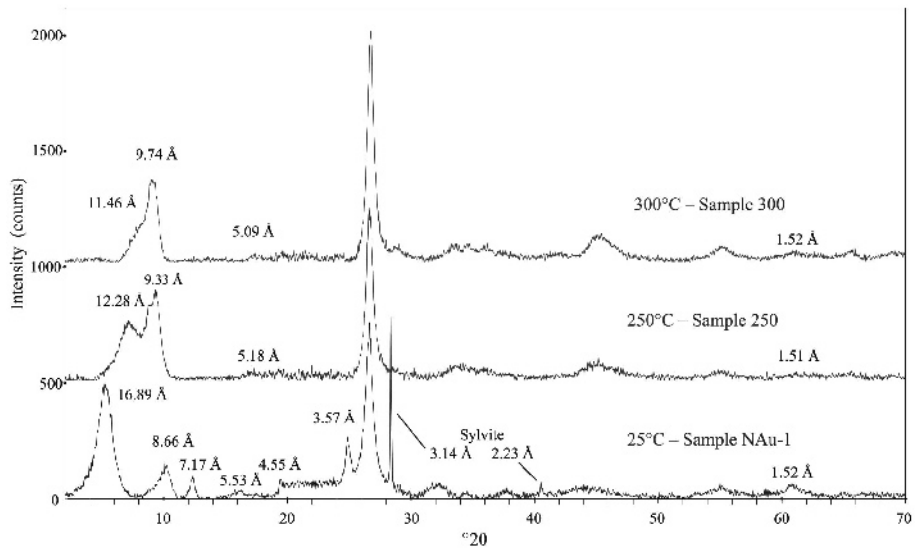

Figure 2. XRD patterns of oriented, ethylene glycol-saturated samples produced by heating NAu-1 with KCl brine in gold capsules at 100 MPa.

https://doi.org/10.1346/CCMN.2012.0600607 Published online by Cambridge University Press

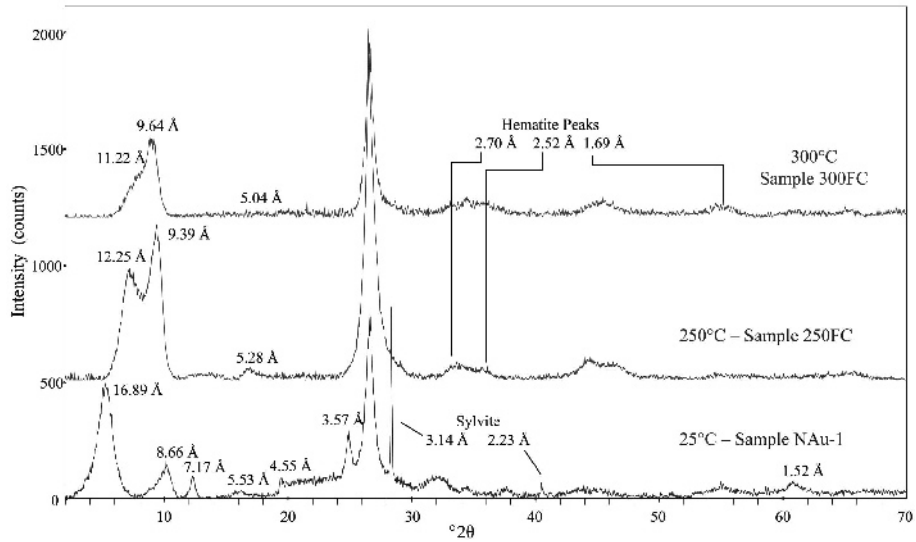

Figure 3. XRD patterns of oriented, ethylene glycol-saturated samples produced by heating NAu-1 with KCl brines and graphite in gold capsules at 100 MPa. Progressive conversion of nontronite and kaolinite to an Fe-rich, mixed-layer clay mineral was consistent at 250ºC and 300ºC, regardless of graphite content, brine composition, or fluid:clay ratio.

phase is better described as ferroceladonite than illite (Figure 6). In the absence of electron microprobe analysis, the bulk composition of the experimental products cannot be constrained precisely, but is probably similar to Fe-celadonite with some degree of Al substitution in both tetrahedral and octahedral sheets, considering the starting bulk composition of the nontronite and kaolinite reactants.

TEM data

Morphology. Examination by TEM of the experimental samples showed trends of increasing grain size, increasing lath-like morphology, and increasing stability in the electron beam with respect to increasing experimental temperature at 100 MPa. Un-reacted NAu-1 consisted of laminated crystal aggregates up to several hundreds of nm in size. Individual crystals were curviplanar, *i.e.* exhibiting 'cornflake' texture, and had crystal terminations typical of smectites (Figure 1) (Henning and Störr, 1986). Kaolinite was conspicuously absent from all images of NAu-1, despite its presence in XRD traces from the same aliquot, except in sample 250 F (Figure 7) where it was also observed in XRD results (Figure 4). Kaolinite is extremely sensitive to the electron beam and

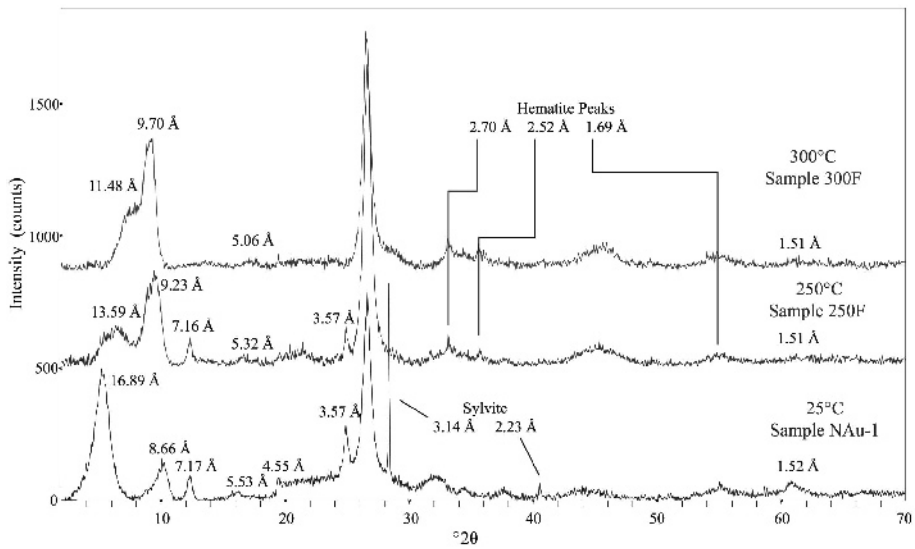

Figure 4. XRD patterns of oriented, ethylene glycol-saturated samples produced by heating NAu-1 with KCl and $FeCl_2$ brines in gold capsules at 100 MPa.

https://doi.org/10.1346/CCMN.2012.0600607 Published online by Cambridge University Press

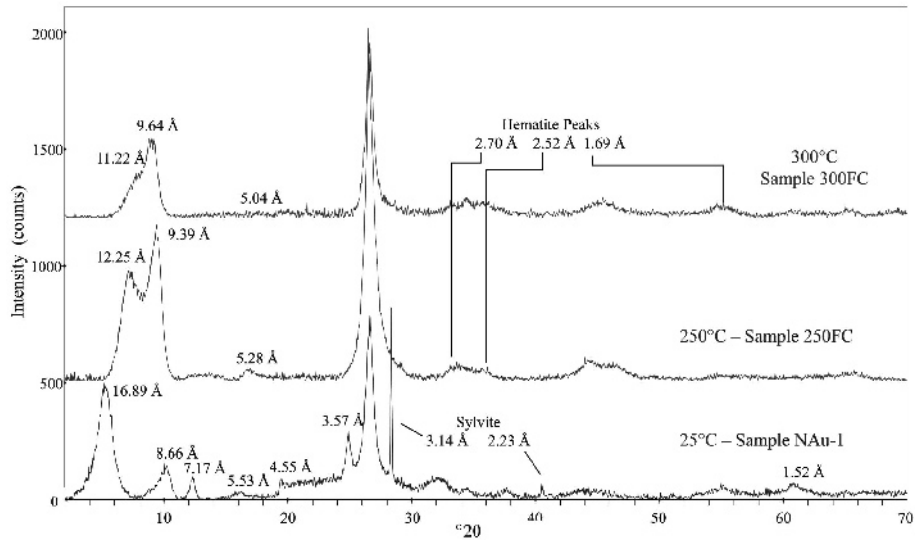

Figure 5. XRD patterns of oriented, ethylene glycol-saturated samples produced by heating NAu-1 with KCl and $FeCl_2$ brines and graphite in gold capsules at 100 MPa.

crystals in sample 250 F 'shimmered' in real time as they decomposed under illumination.

Upon heating to 250ºC, the crystal forms of NAu-1 displayed a pockmarked dissolution texture, and neoformed, euhedrally terminated crystal laths exhibiting aspect ratios of >3:1 appeared (Figure 8a, c, e). The laths formed as individual crystals a few hundred Ångstroms long and in complex bundles resembling sheaved blades of grass on the order of 1 μm long, consistent with experimentally produced I-S "packets" described by Drief *et al*. (2002) and natural samples examined by Dong *et al*. (1997). Further heating to 300ºC resulted in nearly complete dissolution of NAu-1 as well as the lath-like crystals, similar to natural 1*M* celadonite clays examined by Henning and Störr (1986), become the dominant morphology (Figure 8b, d, f, h).

Sample preparation for TEM included numerous disaggregation, stirring, suspension, and centrifugation steps which limit the interpretation of observed crystallite orientations and relationships as accurate representations of the original material. However, images provided substantial visual evidence that 1*M* crystal laths form immediately adjacent and/or attached to crystallites with smectitic character, most notably observed in samples 250F, 250FC, and 300FC (Figure 8e, g, h). In many cases, laths appeared to grow at the expense of the smectite. The observed experimental products were strikingly similar to early TEM studies describing the smectite-1*M* illite-2*M* illite maturation model observed in natural samples (*e.g.* Pollastro, 1985; Inoue *et al.*, 1987).

Non-clay phases, including salts and Fe oxides, were also visible in bright-field images. The salts formed dipyramidal to octahedral crystals ranging from ~10 to several hundred Ångstroms in size that decomposed readily under the electron beam (Figure 8b, e). The Fe-oxide material was present as hazy, globular masses and in samples with added Fe (250 F, 300 F, 250 FC, and 300

Table 2. XRD peak-position data from oriented mounts of ethylene glycol-solvated experimental clay products. Percent illite (% illite) values calculated using Wantanabe's method ($d_{002/003}$) described by Moore and Reynolds (1997), and using the Środoń (1981) method (Δ2θ).

Sample	d_{001} (Å)	$d_{001/002}$ (Å)	$d_{002/003}$ (Å)	% Illite $d_{002/003}$ (Å)	% Illite (Δ2θ)
250	12.28	9.33	5.18	82	77
300	11.46	9.74	5.09	90	88
250 C	12.06	9.50	5.21	80	78
300 C	11.48	9.70	5.06	91	90
250 F	13.59	9.23	5.32	66	61
300 F	11.48	9.70	5.06	91	81
250 FC	12.25	9.39	5.28	72	71
300 FC	11.22	9.64	5.04	92	89

https://doi.org/10.1346/CCMN.2012.0600607 Published online by Cambridge University Press

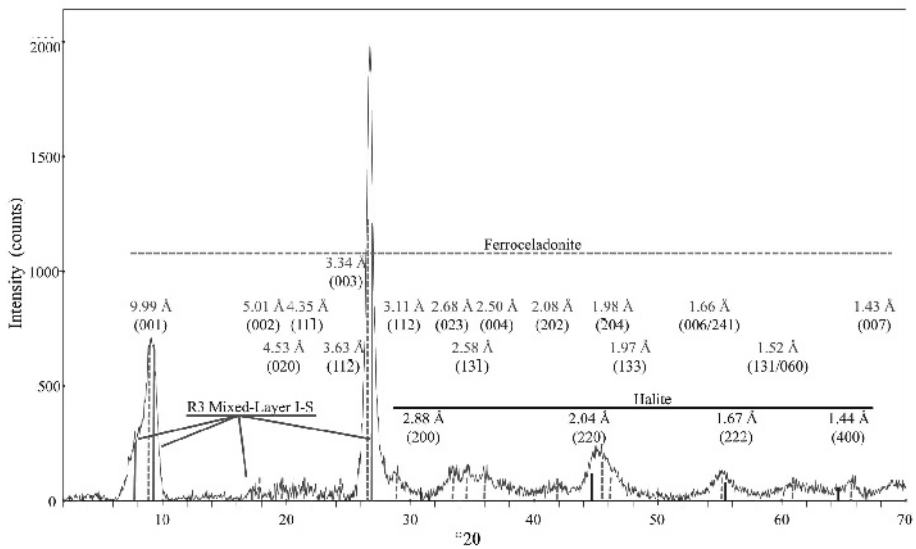

Figure 6. XRD pattern of air-dried sample 300 with Fe-celadonite (dashed peak-bars) and K-bearing halite (black peak-bars) peak overlays, from ICDD PDF 00-054-0782 and 00-026-0918, respectively. *hkl* indices are displayed with peak positions. The presence of a well ordered (R3) mixed-layer expandable/non-expandable clay mineral is indicated by d_{001} peak broadening in the 6−10º2θ range (gray peak-bars). Random orientation due to salt crystallization growth results in *hkl* reflections. The low intensity of the d_{002} and $d_{002/003}$ peaks near 17º2θ is caused by structural Fe (Moore and Reynolds, 1997).

FC), consistent with XRD results for these samples and presumed to be experimental artifacts.

Electron diffraction. Electron diffraction imaging was conducted on purified NAu-1 and all experimental samples, and the results recorded the transition from smectite to Fe-celadonite (Figure 9, Table 3). NAu-1 patterns exhibited complete circular rings with broad bands, a consequence of turbostratic crystal-domain stacking in smectite. Several characteristic spacings from nontronite were identified (Table 3), along with kaolinite rings at 4.20 Å and 2.40 Å, representing the ($\bar{1}\bar{1}$1) and (003) *hkl* planes. A broad doublet band centered at 1.50 Å formed a composite 060 reflection for both nontronite and kaolinite. Similar images of samples heated to 250 and 300ºC were characterized by spotty diffraction rings, a symptom of epitaxial stacking of relatively few crystal domains, each with minor crystallographic rotation relative to adjoining units. Fe-celadonite was indicated in these samples by spotty rings (Figure 9, Table 3). Halite's (222) plane may also have been present in sample 250, given a faint ring at 1.63 Å; however, the ($\bar{3}$14) plane of Fe-celadonite shares a similar spacing. The electron diffraction results are consistent with smectite transitioning to Fe-celadonite with minor salt contamination, considering crystallographic data given by Li *et al.* (1997) and the International Center for Diffraction Data (ICDD) powder diffraction file 00-054-0782.

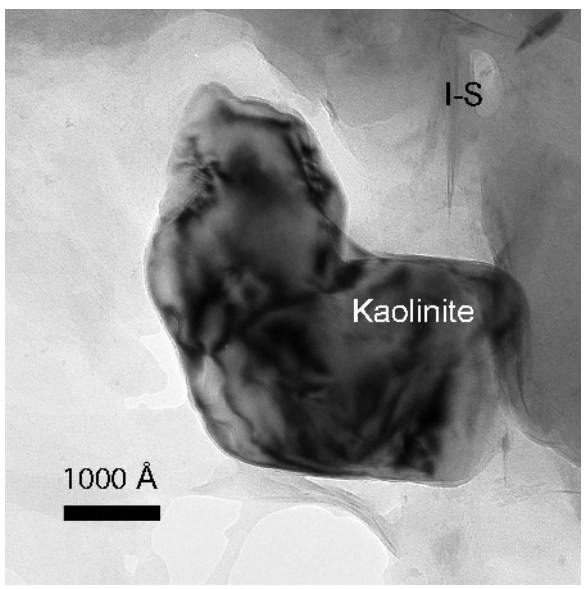

Figure 7. TEM image of kaolinite in sample 250F.

Lattice-fringe imaging. Raw NAu-1, purified NAu-1, samples 250, 300, and 300C were examined at magnifications of 200−500 kX. Sectioned NAu-1 consisted of sinuous bundles of crystalline laminae 12−13 Å thick. The bundles terminated irregularly in the *a-b* crystallographic plane, featured poorly defined d_{00l} terminations, and ranged in thickness from 2 to >20 laminae (Figure 10a). Raw and purified preparations of NAu-1 showed no appreciable difference in lattice spacing. Samples 250 and 300 consisted of lineated crystal bundles with well defined terminations in all crystal dimensions. Each bundle ranged between ~2 and 10 d_{00l} planes thick (Figure 10b), with a few containing up to

https://doi.org/10.1346/CCMN.2012.0600607 Published online by Cambridge University Press

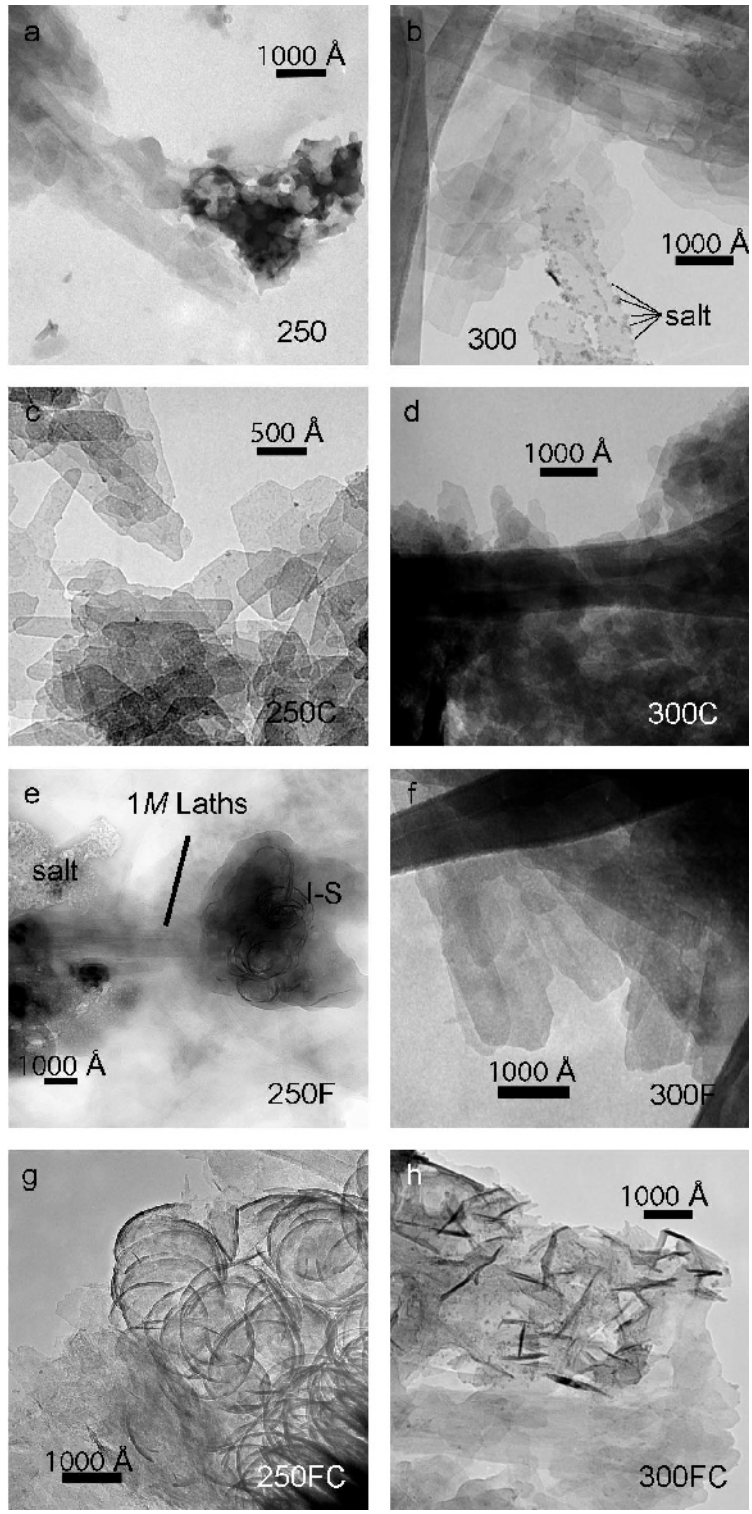

Figure 8. TEM images of experimental samples produced by heating NAu-1 with KCl brine in gold capsules at 100 MPa for 2 weeks. 250ºC samples contained mixed-layer clay minerals with pockmarked dissolution textures and semicircular crystal bundles intimately associated with neoformed 1*M* crystal laths (a, c e, g). 300ºC samples consisted predominantly of lath-shaped crystals, with only minor remnants of particles of smectitic character (b, d, f, h). Rounded, vermiform crystal bundles were observed in all experimental runs, but were best imaged in samples 250FC and 300FC (g, h). Encrusting crystals of halite, as observed in sample 300, were present to varying degrees in all samples (*e.g.* 'salt' in parts b and f).

https://doi.org/10.1346/CCMN.2012.0600607 Published online by Cambridge University Press

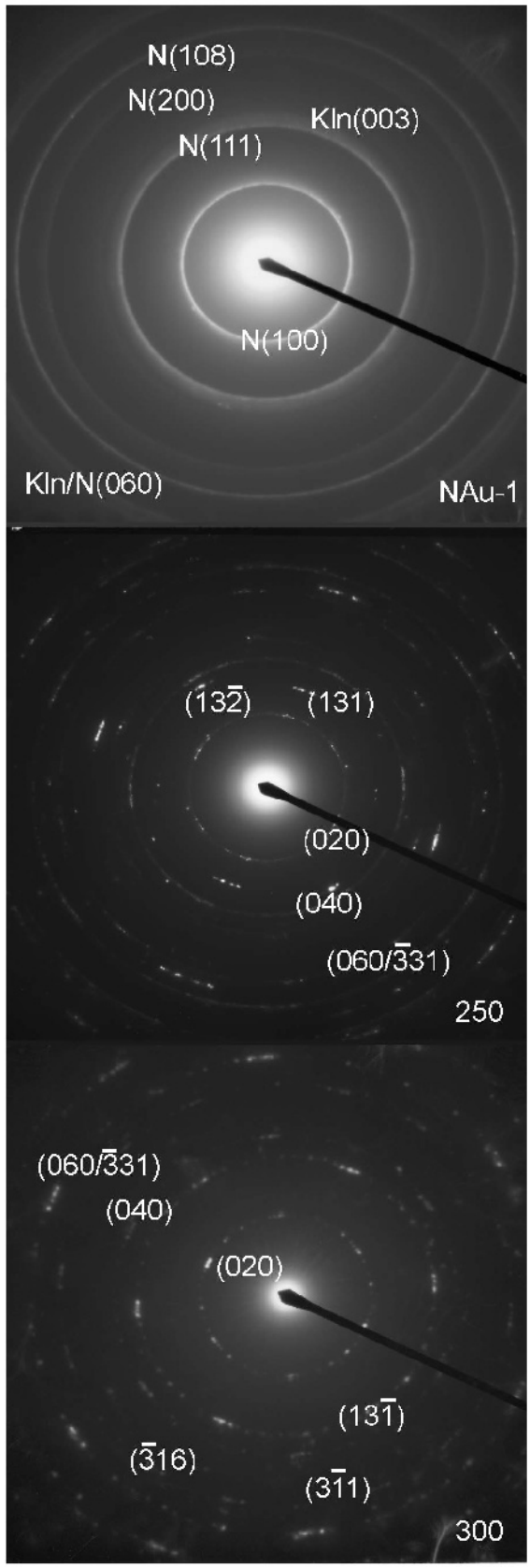

20 planes. Samples heated to 250ºC generally had fewer laminae than those heated to 300ºC, consistent with continued growth of the 1*M* crystals throughout the experiment.

Lattice fringes in the heated samples ranged in thickness depending on the location within each crystalline bundle. Laminae at the outer edges of bundles had lattice spacings of ~11 Å, but <10 Å at the center of the bundles. Ahn and Peacor (1989) cited experimental conditions and chemical variation within I-S packets to explain illitic interlayer spacings which were not equal to exactly 10 Å. Bundles with expandable smectitic outer layers as observed in samples 250, 300, and 300 C are consistent with observations of natural I-S samples by Murakami *et al.* (2005).

Measurement by TEM of clay basal lattice fringes indicated general trends but should not be considered a definitive phase identification tool. Minor variation in section thickness, resin intercalation, resin quality, section size, and clay crystallite orientation within the resin all affect measurement quality. In practice, resin and clay are extremely difficult to section uniformly, because of differential hardness between the clay and resin. The beam interacts with nominally thick sections, causing sample drift, resin warp or vaporization, and/or nearly instantaneous clay-crystal decomposition in the electron optical column. Where clay materials in the correct orientation were present, but contained overlaps more than a few crystalline units thick, Moiré fringes obscured the true basal spacing. Very thin sections are the best to image, but are prone to sag in the TEM grids. Sagging sections result in a deep focal range in a given lateral area, compounding alignment errors such as lens astigmation. Focal setting, optimized at a slight overfocus (in contrast to conventional TEM imaging) is extremely important to resolving the fine variation in grayscale necessary to define the difference between a 'good' fringe, and an unusable one (Guthrie and Veblen, 1989; Veblen *et al.*, 1990). Compounding the technical difficulties in making realistic and accurate lattice-fringe measurements, the phyllosilicates illite, celadonite, glauconite, and their mixed-layer combinations are essentially identical, especially when the point-to-point resolution of the instrument is 10% of the intended measurement.

EDS. Energy dispersive spectroscopy was performed on NAu-1, sample 250, and on sample 300 to assess the relative retention of Fe in the experimental products. A significant Fe signal was produced in each sample, while analysis of an empty TEM grid did not contain any Fe. Therefore, Fe remained a structural component in

Figure 9. Electron diffraction images of untreated NAu-1 and experimental phyllosilicates 250 (250ºC) and 300 (300ºC) (for an explanation see the text). N = nontronite, Kln = kaolinite.

https://doi.org/10.1346/CCMN.2012.0600607 Published online by Cambridge University Press

Table 3. Clay mineral electron diffraction data.

(*hkl*)	NAu-1[1] *d* (Å)	NAu-1 observed, *d* (Å)	(*hkl*)	Fe-Cel[2] *d* (Å)	250 *d* (Å)	300 *d* (Å)
(100)	4.55	4.47	(020)	4.53	4.54	4.50
(111)	2.60	2.58	(13$\bar{1}$)	2.58	2.58	2.58
			(13$\bar{2}$)	2.40		2.42
(200)	2.28	2.26	(040)	2.26	2.24[4]	2.26
(108)	1.72	1.71	($\bar{3}$11)	1.72	1.70	1.71
	1.52		($\bar{3}$31)/(060)	1.51[3]	1.50[3]	1.52[3]
			($\bar{3}$16)	1.31		1.32

References: [1] Keeling *et al*. (2000); [2] ICDD PDF 00-054-0782. [3] nontronite and kaolinite doublet (060) average 1.51 Å; [4] average of poorly resolved doublet, 2.28 Å (040) and 2.20 Å (041) diffraction rings.

samples 250 and 300. The EDS analysis also identified areas consisting primarily of Na and Cl, assumed to be halite as observed in XRD patterns and TEM bright-field images, or K and Cl, assumed to be sylvite (Figure 8e). Spots were chosen for analysis based on the ability to visually discriminate the material being sampled by the beam, *i.e.* smectitic clay, illitic clay, or salt. Atomic number (*Z*) corrections were applied to the raw count data in an attempt to determine the relative proportions of Fe, Si, and Al NAu-1 and experimentally produced clays (Lorimer, 1978). Because of the beam sensitivity of target clays, considerable alteration, if not complete destruction, of the sample spot occurred during analysis, and was reflected by low count rates, even when sampling times were reduced to the minimum. Given the degree of sample decomposition in the beam, and the fact that the analysis was standardless, quantitative analysis *via* EDS was not possible. The extent to which EDS analysis was useful for this study was to indicate that Fe was retained within the 2:1 phyllosilicate phases throughout the experiment.

Aqueous chemistry

A sample of NAu-1 soaked in 2 M KCl brine at ambient conditions for the same duration as the other samples served as a control. After correcting for the blank and control sample, the supernatant from sample 250 contained 39.5 µg/L Al, 2862.0 µg/L Si, and 5597.0 µg/L Fe, the highest concentrations of all the samples tested: representing 0.02%, 1.11%, and 2.08% of the available Al, Si, and Fe present in the original NAu-1, respectively (Table 4). The low target analyte concentrations dissolved during the course of the experiment were consistent with the XRD analysis, indicating that Al, Si, and Fe were readily incorporated into the crystalline phases observed in the TEM.

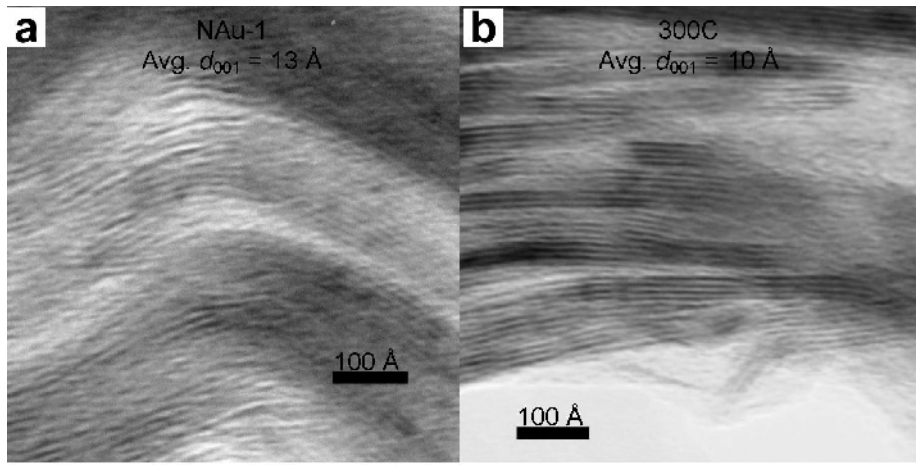

Figure 10. TEM lattice-fringe images of NAu-1 (a) and sample 300C (b). Both images were collected at 500 kX, are displayed at the same scale, and are consistent with thin-sectioned natural smectite and I-S mixed-layer clay minerals in LR White resin (Dong *et al*., 1997). NAu-1 interlayer spacing averages 13 Å (a). The bundles of mixed-layer clay minerals are 5–15 domains thick, and the lattice spacing at the exterior of the bundles typically approaches those seen in the nontronite, but those within each bundle are <10 Å (b).

https://doi.org/10.1346/CCMN.2012.0600607 Published online by Cambridge University Press

Table 4. Experimental fluid ICP-MS results. Percentages of Al, Si, and Fe refer to the mass percentage of structural Fe mobilized from the pre-experiment aliquot of NAu-1 to the experimental fluid for each sample.

Sample	Al (μg/L)	Al (%)	Si (μg/L)	Si (%)	Fe (μg/L)	Fe (%)
300	73.5	0.02	1,711.0	0.45	5,610.8	1.41
250	162.6	0.06	2,891.3	1.11	5,616.2	2.08
250 C	63.7	0.04	915.6	0.68	1,105.0	0.79
NAu-1	123.1	0.05	29.4	0.01	19.1	0.01

The mass percentage is based on the NAu-1 structural formula $K_{1.05}[Al_{.29}Fe_{3.68}Mg_{.04}][Si_{6.98}Al_{1.02}]O_{20}(OH)_4$ defined by Keeling *et al*. (2000).

DISCUSSION

The present study tracked the fate of a CBD-cleaned nontronite starting material under hydrothermal conditions, including temperatures up to 300ºC with 1 M KCl. The results demonstrated that Fe-rich smectites pass through a similar alteration sequence of mixed-layer to discrete phases as observed in more aluminous clays. However, despite having two sources of aluminum (structural Al from the nontronite and released from the decomposition of kaolinite), celadonite-type rather than illite-type 10 Å clays were formed. The addition of graphite and/or ferrous chloride solution had no measurable effect. The Fe was retained in the phyllosilicate phases. Fe-celadonite, or any solid solution composition containing mixed-valence Fe, should only be stable within the magnetite stability field (Velde, 1972). The oxidation state of Fe in the nontronite was largely 3+ when loaded in the tube. Despite reducing conditions in the cold-seal capsules by the end of the experiments, precipitation of magnetite was not observed.

Both celadonites and illites belong to the collection of 10 Å dioctahedral phyllosilicates with non-exchangeable interlayer cations that includes glauconites, sericites, phengites, *etc.* that are inclusively referred to as illitic when present in the $\leqslant 2$ μm size fraction of sedimentary rocks (Meunier and Velde, 2004). In the sense that glauconites are connected to the marine water–sediment interface, the term celadonite also implies geologic setting significance, as it often precipitates as fracture fill and vein fill in ancient hydrothermal vents (Odin, 1988). While the experimental products of this study are not octahedral Al-rich 'illite' in the strictest sense, their formation is significant in that upon exposure to burial conditions, a smectite was progressively altered to an Fe-rich 1*M* polytype 10 Å clay.

Crystal chemical considerations play a role in determining which 2:1 phyllosilicate phase will crystallize. Meunier and Velde (2004) cautioned that the traditional Al- and Mg-rich "illite" is only a single composition belonging to a family of 10 Å 2:1 layer dioctahedral clay minerals whose layer charge is defined by the endmembers celadonite (octahedrally negative), muscovite (tetrahedrally negative), and pyrophyllite (no net layer charge). The celadonite-like octahedral substitutions create the negative charge by 1:1 divalent:trivalent cation substitution pairs: Fe^{2+}:Fe^{3+}, Mg:Fe^{3+}, Mg:Al, and Fe^{2+}:Al with nearly full Si occupancy in the tetrahedral sheet, and very little Al. Nearly complete solid solution exists between substitution pairs in celadonites (Li *et al.*, 1997). This solid solution does not occur with respect to octahedral Fe and Al between celadonites and illites because of the strain induced by the different Fe and Al ionic radii as tetrahedral substitution for Si increases (Li *et al.*, 1997; Meunier, 2005; Drits *et al*., 2010). Where intermediate Fe^{2+} and Al octahedral substitution between celadonite and illite does result in a stable structure, increasing Al content reduces the negative layer charge to 1.5−1.8 per unit cell, and reduces interlayer K occupancy (Longuépée and Cousineau, 2006).

Evidence from this study supports both the solid-state transformation and dissolution-precipitation models of illitization, through the creation of both mixed-layer and coexisting discrete 10 Å clay minerals. When held at burial temperatures and pressure, XRD analyses indicated initial dissolution of kaolinite and the formation of mixed-layer clay, followed by increasing order of the mixed-layer phase and concurrent precipitation of ferroceladonite. Chemical gradients as described by McCarty *et al.* (2008, 2009) and Lanson *et al.* (2009) can be used to explain in a general sense the process which was probably occurring within the experiment. Kaolinite dissolution solvated K, Al, and Si; these components were then available to reorder the octahedral sheets *via* 'lateral' solid-state transfer, expelling Fe and H_2O from the structure and fixing interlayer K (Olives *et al.*, 2000). Upon consumption of the kaolinite dissolution products, the dissolution of remaining smectite and newly formed mixed-layer clay minerals then provided media and a phyllosilicate template for 1*M* polytype crystal growth, as seen in experimental TEM images. The formation of Fe-celadonites rather than high-aluminum illite was a result of the chemical gradient present in the experiment. In terms of the closed synthetic system created for this experiment, the preponderance of K and Fe in the system after mixed-

https://doi.org/10.1346/CCMN.2012.0600607 Published online by Cambridge University Press

layer transformation, with a fixed supply of Si and essentially no Al, resulted in an Fe-rich celadonite ($K_2(Fe^{2+})_2(Fe^{3+})_2Si_8O_{20}(OH)_4$) phase.

In addition, a critical reaction parameter that this study could not duplicate was time. Perhaps Fe-bearing clays form more rapidly, then convert to Al-rich forms over time. Transformations observed in this study with nontronite as the starting material proceeded much faster than those observed at similar temperatures, brine compositions, and solid/fluid ratios by Ferrage *et al*. (2011) with SWy-2 montmorillonite as the starting material. Güven and Huang (1991) precipitated mixed-layer I-S hydrothermally from synthetic gels. Gels substituting some Fe for Al resulted in I-S with 0.6 $Fe^{3+}/Si_8O_{20}(OH)_4$, and resulted in quicker precipitation than gels with similar Mg substitution or no substitution for Al.

Some evidence for rapid precipitation of Fe-rich phyllosilicates followed by slow transition to aluminum-rich clays can also be found from studies of natural systems. Redox cycling forced by subaerial weathering in saline lacustrine settings has been shown to result in octahedral Fe incorporation in illite of up to 2.32 Fe/$Si_8O_{20}(OH)_4$ (Huggett *et al.*, 2001). Dainyak *et al.* (2006) conducted a Mössbauer and infrared spectroscopy study of a sequence of natural shales and observed progressive Fe and Mg replacement by Al through diagenesis, citing a solid-state alteration mechanism linking clay diagenesis to hydrocarbon maturation as proposed by Lindgreen *et al.* (2000). Also, Lynch *et al.* (1997) linked the increasingly reduced character of octahedral Fe with increasing depth (1.8–3.7 km) in the Frio Formation to increasing Al-for-Mg substitution in the octahedral sheet.

Celadonites are not typically seen in the diagenetic alteration of terrigenous sediments, probably because of the presence of Al-rich fluids sourced from dissolution of feldspar and low- Fe-clay phases. High Al activity relative to Fe may be critical to the formation of an aluminous illite. Additional experimental synthesis based on this work, including diagenetically relevant Al concentrations present in brines and/or a proportionately large kaolinite component, may further clarify the relationship between clay diagenesis and magnetite precipitation.

On the other hand, celadonite-type clay minerals rather than illite-type clay minerals are common alteration products of basaltic rocks. Oxygen fugacity appears to have little effect on celadonite stability (Wise and Eugster, 1964). It formed in reducing conditions in this work, but also forms in oxidizing environments within oceanic crust. Thus, the sequence of alteration observed in this study might help to explain the role of temperature in aqueous alteration on Mars. Meunier *et al.* (2010) proposed that Fe-rich clay microsystems in weathered basal-komatiite lavas serve as an analog for early Earth and Mars clay-forming environments. In the present study, only 2 weeks at temperatures >250ºC were required to convert nontronite extensively to mixed-layer clay and celadonite. Given the great abundance of nontronites on Mars, the presence of celadonite would serve as an indicator for hydrothermal alteration. Additionally, distinguishing between illite-type and celadonite-type clay minerals could indicate whether or not Al was mobilized outside of localized reaction environments.

ACKNOWLEDGMENTS

The authors thank Dr David London and the University of Oklahoma's Experimental Geochemistry Laboratory, Dr Scott Russell and the University of Oklahoma's Sam Roberts Noble Electron Microscopy Laboratory, and Dr Qinhong Hu at the University of Texas-Arlington for their assistance during this project. Without access to their facilities, equipment, and expertise this work would not have been possible. The authors are very grateful for the efforts of two reviewers and of Dr Stucki, whose comments significantly improved the manuscript.

REFERENCES

Abercrombie, H., Hutcheson, I., Bloch, J., and de Caritat, P. (1994) Silica activity and the smectite illite reaction. *Geology*, **22**, 539–542.

Ahn, H. and Peacor, D.R. (1986) Transmission and analytical electron microscopy of the smectite-to-illite transition. *Clays and Clay Minerals*, **34**, 165–179.

Allen, V.T. and Scheid, V.E. (1946) Nontronite in the Columbia river region. *American Mineralogist*, **31**, 294–312.

Altaner, S.P. and Ylagan, R.F. (1997) Comparison of structural models of mixed-layer illite/smectite and reaction mechanisms of smectite illitization. *Clays and Clay Minerals*, **45**, 517–533.

Andrews, A.J. (1980) Saponite and celadonite in layer 2 basalts, DSDP Leg 37. *Contributions to Mineralogy and Petrology*, **73**, 323–340.

Banerjee, S., Elmore, R.D., and Engel, M.H. (1997) Chemical remagnetization and burial diagenesis: Testing the hypothesis in the Pennsylvanian Belden Formation, Colorado. *Journal of Geophysical Research*. **102**, 24,825–24,842.

Bartels, J.M., editor (1996) *Methods of Soil Analysis: Part 3 Chemical Methods.* Soil Science of America, Madison, Wisconsin.

Blumstein, A.M., Elmore, R.D., Engel, M.H., Elliot, C., and Basu, A. (2004) Paleomagnetic dating of burial diagenesis in Mississippian carbonates, Utah. *Journal of Geophysical Research*, **109**, 1–16.

Brothers, L.A., Engel, M.H., and Elmore, R.D. (1996) The late diagenetic conversion of pyrite to magnetite by organically complexed ferric iron. *Chemical Geology*, **130**, 1–14.

Chevrier, V., Poulet, F., and Bibring, J.-P. (2007) Early geochemical environment of Mars as determined from thermodynamics of phyllosilicates. *Nature*, **448**, 60–63.

Chipera, S. and Bish, D. (2001) Baseline studies of the Clay Minerals Society Source Clays: Powder X-ray diffraction analyses. *Clays and Clay Minerals*, **49**, 398–409.

Cogoini, M. (2001) Magnetic minerals: Understanding the processes of formation in soils and clays and identifying their presence in the rock record. PhD thesis, University of Oklahoma, Norman, Oklahoma, USA.

D'Antonio, M. and Kristensen, M.B. (2005) Hydrothermal alteration of oceanic crust in the West Phillippine Sea Basin

(Ocean Drilling Program Leg 195, Site 1201): inferences from a mineral chemistry investigation. *Mineralogy and Petrology*, **83**, 87–112.

Dainyak, L.G., Drits, V.A., Zviagina, B.B., and Lindgreen, H. (2006) Cation redistribution in the octahedral sheet during diagenesis of illite-smectites from Jurassic and Cambrian oil source rock shales. *American Mineralogist*, **91**, 589–603.

Dekov, V.M., Kamenov, G.D., Stummeyer, J., Thiry, M., Savelli, C., Shanks, W.C., Fortin, D., Kuzmann, E., and Vértes, A. (2007) Hydrothermal nontronite formation at Eolo Seamount (Aeolian volcanic arc, Tyrrhenian Sea). *Chemical Geology*, **245**, 103–119.

Dennie, D., Elmore, R.D., Deng, J., Manning, E., and Pannalal, J. (2012) Palaeomagnetism of the Mississippian Barnett Shale, Fort Worth Basin, Texas. In: *Remagnetization and Chemical Alteration of Sedimentary Rocks* (R.D. Elmore, A.R. Muxworthy, M. Aldana, and M. Mena, editors). Special Publications, **371**, Geological Society, London (DOI: 10.1144/SP371.10).

Dong, H., Peacor, D., and Freed, R.L. (1997) Phase relations among smectite, R1 illite-smectite, and illite. *American Mineralogist*, **82**, 379–391.

Drief, A., Martinez-Ruiz, F., Nieto, F., and Sanchez, N.V. (2002) Transmission electron microscopy of smectite in K-enriched seawater solution at 50ºC and basic pH. *Clays and Clay Minerals*, **50**, 746–756.

Drits, V.A., Zviagina, B.B., McCarty, D.K., and Salyn, A.L. (2010) Factors responsible for crystal-chemical variations in the solid solutions from illite to aluminoceladonite and from glauconite to celadonite. *American Mineralogist*, **95**, 348–361.

Eberl, D.D., Whitney, G., and Khoury, H. (1978) Hydrothermal reactivity of smectite. *American Mineralogist*, **63**, 401–409.

Ehlmann, B.L., Mustard, J.F., Murchie, S.L., Bibring, J.P., Meunier, A., Fraeman, A.A., and Langevin, Y. (2011) Subsurface water and clay mineral formation during the early history of Mars. *Nature*, **479**, 53–60.

Elliott, W.C., Osborn, S., O'Brien, V., Elmore, R.D., Engel, M.H., and Wampler, M. (2006) A comparison of K-Ar ages of diagenetic illite and the age implications of a remagnetization in the Cretaceous Marias River Shale, Disturbed Belt, Montana. *Journal of Geochemical Exploration*, **89**, 92–95.

Elmore, R.D. and Leach, M.C. (1990) Remagnetization of the Rush Springs Formation, Cement, Oklahoma: Implications for dating hydrocarbon migration and aeromagnetic exploration. *Geology*, **18**, 124–127.

Elmore, R.D., Engel, M.H., Crawford, L., Nick, K., Imbus, S., and Sofer, Z. (1987) Evidence for a relationship between hydrocarbons and authigenic magnetite. *Nature*, **325**, 428–430.

Elmore, R.D., Kelley, J., Evans, M., and Lewchuk, M. (2001) Remagnetization and Orogenic Fluids: Testing the hypothesis in the central Appalachians. *Geological Journal International*, **144**, 568–576.

Eslinger, E. and Pevear, D. (1988) *Clay Minerals for Petroleum Geologists and Engineers*. SEPM Short Course No. 22.

Fernández-Caliani, J.C., Crespo, E., Rodas, M., Barrenechea, J.F., and Luque, F.J. (2004) Formation of nontronite from oxidative dissolution of pyrite disseminated in Precambrian felsic metavolcanics of the southern Iberian Massif (Spain). *Clays and Clay Minerals*, **52**, 106–114.

Ferrage, E., Vidal, O., Mosser-Ruck, R., Cathelineau, M., and Cuadros, J. (2011) A reinvestigation of smectite illitization in experimental hydrothermal conditions: Results from X-ray diffraction and transmission electron microscopy. *American Mineralogist*, **96**, 207–223.

Gill, J.D., Elmore, R.D., and Engel, M.H. (2002) Chemical remagnetization and clay diagenesis: Testing the hypothesis in the Cretaceous sedimentary rocks of northwestern Montana, *Physics and Chemistry of the Earth*, **27/25–31**, 1131–1139.

Guthrie, D.G. and Veblen, D.R. (1989) High Resolution Transmission Electron Microscopy of mixed layer illite/smectite: Computer simulation. *Clays and Clay Minerals*, **37**, 1–11.

Güven, N. and Huang, W. (1991) Effects of octahedral Mg and Fe substitutions on hydrothermal illitization reactions. *Clays and Clay Minerals*, **39**, 387–399.

Henning, K. and Störr, M. (1986) *Electron Micrographs (TEM, SEM) of clays and clay minerals*. Akademi-Verlag, Berlin, Germany.

Hirt, A., Banin, A., and Gehring, A. (1993) Thermal generation of ferromagnetic minerals from iron-enriched smectites. *Geophysics Journal International*, **115**, 1161–1168.

Holloway, J.R. (1984) Graphite-CH_4-H_2O-CO_2 equilibria at low-grade metamorphic conditions. *Geology*, **12**, 455–458.

Hower, J., Eslinger, W.V., Hower, M., and Perry, E.A. (1976) Mechanism of burial metamorphism of argillaceous sediments: I. Mineralogical and chemical evidence. *Geological Society of America Bulletin*, **87**, 725–737

Huang, W., Longo, J.M., and Pevear, D.R. (1993) An experimentally derived kinetic model for smectite-to-illite conversion and its use as a geothermometer. *Clays and Clay Minerals*, **41**, 162–177.

Hugget, J.M., Gale, A.S., and Clauer, N. (2001) The nature and origin of non-marine 10 Å clay from the Late Eocene and Early Oligocene of the Isle of Wright (Hampshire Basin), UK. *Clay Minerals*, **36**, 447–464.

Inoue, A. (1983) Potassium fixation by clay minerals during hydrothermal treatment. *Clays and Clay Minerals*, **31**, 81–92.

Inoue, A., Kohyama, N. Kitagawa, R., and Watanabe, T. (1987) Chemical and morphological evidence for the conversion of smectite to illite. *Clays and Clay Minerals*, **35**, 111–120.

Jackson, M., McCabe, C., Ballard, M.M., and Van der Voo, R. (1988) Magnetite authigenesis and diagenetic paleotemperatures across the northern Appalachian basin. *Geology*, **16**, 592–595.

Jaisi, D.P., Dong, H., and Morton, J.P. (2008) Partitioning of Fe(II) in reduced nontronite (NAu-2) to reactive sites: reactivity in terms of Tc(VII) reduction. *Clays and Clay Minerals*, **56**, 175–189.

Jaisi, D.P., Eberl, D.D., Dong, H., and Kim, J. (2011) The formation of illite from nontronite by mesophilic and thermophilic bacterial reaction. *Clays and Clay Minerals*, **59**, 21–33.

Katz, B., Elmore, R.D., Engel, M.H., Cogoini, M., and Ferry, S. (2000) Associations between burial diagenesis of smectite, chemical remagnetization and magnetite authigenesis in the Vocontian Trough of SE-France. *Journal of Geophysical Research*, **105**, 851–868.

Katz, B., Elmore, R.D., Engel, M.H., Cogoini, M., and Ferry, S. (1998) Widespread chemical remagnetization: Orogenic fluids or burial diagenesis of clays? *Geology*, **26**, 603–606.

Keeling, J.L., Raven, M.D., and Gates, W.P. (2000) Geology and characterization of two hydrothermal nontronites from weathered metamorphic rocks at the Uley graphite mine, South Africa. *Clays and Clay Minerals*, **48**, 537–548.

Kennedy, M.J., Pevear, D.R., and Hill, R.J. (2002) Mineral surface control of organic carbon in black shale. *Science*, **295**, 657–660.

Kim, J., Furukawa, Y., Daulton, T.L., Lavoie, D., and Newell, S.W. (2003) Characterization of microbially Fe(III)-reduced nontronite: environmental cell-transmission electron microscopy study. *Clays and Clay Minerals*, **51**, 382–389.

Kim, J., Dong, H., Seabaugh, J., Newell, S.W., and Eberl, D.D. (2004) Role of microbes in the smectite-to-illite reaction. *Science*, **303**, 830–832.

Köhler, B., Singer, A., and Stoffers, P. (1994) Biogenic nontronite from marine white smoker chimneys. *Clays and Clay Minerals*, **42**, 689–701.

Kostka, J.E., Haefele, E., Viehweger, R., and Stucki, J.W. (1999) Respiration and dissolution of iron(III)-containing clay minerals by bacteria. *Environmental Science & Technology*, **33**, 3127–3133.

Lanson, B., Sakharov, B.A., Claret, F., and Drits, V. (2009) Diagenetic smectite-to-illite transition in clay-rich sediments: A reappraisal of X-ray diffraction results using the multispecimen method. *American Journal of Science*, **309**, 476–516.

Li, G., Peacor, D.R., Coombs, D.S., and Kawachi, Y. (1997) Solid solution in the celadonite family: The new minerals ferroceladonite $K_2(Fe^{2+})_2(Fe^{3+})_2Si_8O_{20}(OH)_4$, and ferroaluminoceladonite, $K_2(Fe^{2+})_2Al_2Si_8O_{20}(OH)_4$. *American Mineralogist*, **82**, 503–511.

Li, Y., Vali, H., Sears, S.K., Yang, J., Deng, B., and Zhang, C.L. (2004) Iron reduction and alteration of nontronite NAu-2 by a sulfate-reducing bacterium. *Geochimica et Cosmochimica Acta*, **68**, 3251–3260.

Lindgreen, H., Drits, V.A., Sakharov, B.A., Salyn, A.L., Wrang, P., and Dainyak, L.G. (2000) Illite-smectite structural changes during metamorphism in black Cambrian Alum shales from the Baltic area. *American Mineralogist*, **85**, 1223–1238.

Longuépée, H. and Cousineau, P.A. (2006) Constraints on the genesis of ferrian illite and aluminum-rich glauconite: potential impact on sedimentology and isotopic studies. *The Canadian Mineralogist*, **44**, 967–980.

Lorimer, G. (1987) Quantitative X-ray microanalysis of thin specimens in the transmission electron microscope; a review. *Mineralogical Magazine*, **51**, 49–60.

Lovley, D.R. and Chapelle, F.H. (1995) Deep surface microbial processes. *Reviews of Geophysics*, **33**, 365–381.

Lynch, F.L., Mack, L.E., and Land, L.S. (1997) Burial diagenesis of illite/smectite in shales and the origin of authigenic quartz and secondary porosity in sandstones. *Geochimica et Cosmochimica Acta*, **61**, 1995–2006.

Mas, A., Meunier, A., Beaufort, D., Patrier, P., and Dudoignon, P. (2008) Clay minerals in basalt-hawaiite rocks from Mururoa Atoll (French Polynesia). I. Mineralogy. *Clays and Clay Minerals*, **56**, 711–729.

McCabe, C., Van der Voo, R., Peacor, D.R., Scotese, C.R., and Freeman, R. (1983) Diagenetic magnetite carries ancient yet secondary remanence in some Paleozoic sedimentary carbonates. *Geology*, **11**, 221–223.

McCabe, C., Sassen, R., and Saffer, B. (1987) Occurrence of secondary magnetite within biodegraded oil. *Geology*, **15**, 7–10.

McCarty, D.K., Sakharov, B.A., and Drits, V.A. (2008) Early clay diagenesis in gulf coast sediments: New insights from XRD profile modeling. *Clays and Clay Minerals*, **56**, 359–379.

McCarty, D.K., Sakharov, B.A., and Drits, V.A. (2009) New insights into smectite illitization: A zoned K-bentonite revisited. *American Mineralogist*, **94**, 1653–1671.

Meunier, A. (2005) *Clays*. Springer, Berlin, 472 pp.

Meunier, A. and Velde, B. (2004) *Illite*. Springer, Berlin, 286 pp.

Meunier, A., Petit, S., Cockell, C.S., El Albani, A., and Beaufort, D. (2010) The Fe-rich clay microsystems in basalt-komatiite lavas: importance of Fe-smectites for prebiotic molecule catalysis during the Hadean Eon. *Origin of Live and Evolutionary Biospheres*, **40**, 253–272.

Moore, D.M. and Reynolds, R.C. (1997) *X-ray Diffraction and the Identification of Clay Minerals*. Oxford University Press, New York, 371 pp.

Moreau, M.G., Adera, M., and Enkin, R.J. (2005) The magnetization of clay-rich rocks in sedimentary basins: low-temperature experimental formation of magnetic carriers in natural samples. *Earth and Planetary Science Letters*, **230**, 193–210.

Murakami, T., Inoue, A., Lanson, B., Meunier, A., and Beaufort, T. (2005) Illite-smectite mixed layer minerals in the hydrothermal alteration of volcanic rocks: II. One dimensional High Resolution Transmission Electron Microscopy structure images and formation mechanisms. *Clay and Clay Minerals*, **53**, 440–451.

Mustard, J.F., Murchie, S.L., Pelkey, S.M., Ehlmann, B.L., Milliken, R.E., Grant, J.A., Bibring, J.P., Poulet, F., Bishop, J., Dobrea, E.N., Roach, L., Seelos, F., Arvidson, R.E., Wiseman, S., Green, R., Hash, C., Humm, D., Malaret, E., McGovern, J.A., Seelos, K., Clancy, T., Clark, R., Marais, D.D., Izenberg, N., Knudson, A., Langevin, Y., Martin, T., McGuire, P., Morris, R., Robinson, M., Roush, T., Smith, M., Swayze, G., Taylor, H., Titus, T., and Wolff, M. (2008) Hydrated silicate minerals on Mars observed by the Mars Reconnaissance Orbiter CRISM instrument. *Nature*, **454**, 305–309.

Odin, G.S. (1988) *Developments in Sedimentology: Green Marine Clays*. Elsevier, Amsterdam.

Odom, I.E. (1984) Glauconite and celadonite minerals. Pp. 545–572 in: *Micas* (S.W. Bailey, editor). Reviews in Mineralogy, **13**, Mineralogical Society of America, Washington, D.C.

Olives, J., Amouric, M., and Perbost, R. (2000) Mixed layering of illite-smectite: Results from high-resolution transmission electron microscopy and lattice-energy calculations. *Clays and Clay Minerals*, **48**, 282–289.

O'Reilly, S.E., Watkins, J., and Furukawa (2005) Secondary mineral formation associated with respiration of nontronite, NAu-1 by iron reducing bacteria. *Geochemical Transactions*, **6**, 67–76.

Paul, H.J., Gillis, K.M., Coggon, R.M., and Teagle, D.A.H. (2006) ODP Site 1224: A missing link in the investigation of seafloor weathering. *Geochemistry Geophysics Geosystems*, **7**Q02003, doi:10.1029/2005GC001089.

Pevear, D.R. (1999) Illite and hydrocarbon exploration. *Proceedings of the National Academy of Sciences, U.S.A.*, **96**, 3440–3446.

Pollastro, R.M. (1985) Mineralogical and morphological evidence for the formation of illite at the expense of illite/smectite. *Clays and Clay Minerals*, **33**, 265–274.

Potter, P., Maynard, J., and Depetris, P. (2005) *Mud and Mudstones: Introduction and Overview*. Springer, New York, pp. 128–154.

Rask, J.H., Bryndzia, L.T., Braunsdorf, N.R., and Murray, T.E. (1997) Smectite illitization in Pliocene-age Gulf of Mexico Mudrocks. *Clays and Clay Minerals*, **45**, 99–109.

Ribeiro, F.R., Fabris, J.D., Kostka, J.E., Komadel, P., and Stucki, J.W. (2009) Comparisons of structural iron reduction in smectites by bacteria and dithionite: II. A variable-temperature Mössbauer spectroscopic study of Garfield nontronite. *Pure and Applied Chemistry*, **81**, 1499–1509.

Seyfried, Jr., W.E. and Bischoff, J.L. (1979) Low temperature basalt alteration by seawater: an experimental study at 70ºC and 150ºC. *Geochimica et Cosmochimica Acta*, **43**, 1937–1947.

Środoń, J. (1980) Precise identification of illite/smectite interstratifications by X-ray powder diffraction. *Clays and Clay Minerals*, **28**, 401–411.

Stucki, J.W. (2011) A review of the effects of iron redox cycles on smectite properties. *Comptes Rendus Geoscience*, **343**, 199–209.

Stucki, J.W. and Kostka, J.E. (2006) Microbial reduction of iron in smectite. *Comptes Rendus Geoscience*, **338**, 468–475.

Suk, D., Van der Voo, R., and Peacor, D.R. (1990a) Scanning and transmission electron microscope observations of magnetite and other iron phases in Ordovician carbonates from east Tennessee. *Journal of Geophysical Research*, **95**, 12,327–12,336.

Suk, D., Peacor, D.R., and Van der Voo, R. (1990b) Replacement of pyrite framboids by magnetite in limestone and implications for paleomagnetism. *Nature*, **345**, 611–613.

Tohver, E., Weil, A.B., Solum, J.G., and Hall, C.M. (2008) Direct dating of carbonate remagnetization by $^{40}Ar/^{39}Ar$ analysis of the smectite–illite transformation. *Earth and Planetary Science Letters*, **274**, 524–530.

Ulrey, A.L. and Drees, R.L., editors (2008) *Methods of Soil Analysis: Part 5 – Mineralogical Methods*. Soil Science Society of America, Madison, Wisconsin. USA.

Velde, B. (1972) Celadonite Mica: Solid solution and stability. *Contributions to Mineralogy and Petrology*, **37**, 235–247.

Veblen, D.R., Guthrie, D.G., Livi, K.J.T., and Reynolds, R.C. (1990) High-resolution transmission electron microscopy and electron diffraction of mixed layer illite-smectite: Experimental results. *Clays and Clay Minerals*, **38**, 1–13.

Vorhies, J.S. and Gaines, R.R. (2009) Microbial dissolution of clay minerals as a source of iron and silica in marine sediments. *Nature Geoscience*, **2**, 221–225.

Weaver, C.E. (1960) Possible uses of clay minerals in search for oil. *American Association of Petroleum Geologists Bulletin*, **44**, 1505–1518.

Weil, A.B. and Van der Voo, R. (2002) Insights into the mechanism for orogen-related carbonate remagnetization from growth of authigenic Fe-oxide: A scanning electron microscopy and rock magnetic study of Devonian carbonates from northern Spain. *Journal of Geophysical Research*, **107**, 2063.

Wise, W.S. and Eugster, H.P. (1964) Celadonite: synthesis, thermal stability and occurrence. *American Mineralogist*, **49**, 1031–1083.

Woods, S., Elmore, R.D., and Engel, M. (2002) Paleomagnetic dating of the smectite-to-illite conversion: testing the hypothesis in Jurassic sedimentary rocks, Skye, Scotland. *Journal of Geophysical Research*, **107**, 2091, doi:10.1029/2000JB000053.

Zegers, T.E., Dekkers, M.J., and Bailly, S. (2003) Late Carboniferous to Permian remagnetization of Devonian limestones in the Ardennes: Role of temperature, fluids, and deformation. *Journal Geophysical Research*, **108**, *2357*, doi: 10.1029/2002JB002213.

Zhang, G., Kim, J., Dong, H., and Sommer, A.J. (2007) Microbial effects in promoting the smectite to illite reaction: Role of organic matter intercalated in the interlayer. *American Mineralogist*, **92**, 1401–1410.

Zwing, A., Clauer, N., Liewig, N., and Bachtadse, V. (2009) Identification of remagnetization processes in Paleozoic sedimentary rocks of the northeast Rhenish Massif in Germany by K/Ar dating and REE tracing of authigenic illite and Fe oxides. *Journal of Geophysical Research*, **114**, B06104, doi:10.1029/2008JB006137.

(*Received 20 June 2012; revised 8 December 2012; Ms. 680; W. Huff*)